

Analysis of finite element refinement and order in temporal interference electrical brain stimulation.

Brian J. Tilleria¹ and Mariano Fernández-Corazza¹

¹ Instituto de Investigaciones en Electrónica, Control y Procesamiento de Señales - LEICI (UNLP-CONICET), Facultad de Ingeniería, Universidad Nacional de La Plata, Argentina.

{tilleria.brian, marianof.corazza}@ing.unlp.edu.ar

Abstract. This study investigates the impact of mesh refinement and polynomial interpolation order on the accuracy of finite element method (FEM) simulations of temporal interference (TI) brain stimulation. A multilayer spherical head model was employed, and an analytical solution was derived to compute the relative error in the estimated maximum modulation amplitude within a predefined region of interest (ROI). Six mesh configurations were compared, combining uniform and locally refined meshes with linear (P1) and quadratic (P2) elements. Results show that local refinement near current injection sites significantly improves accuracy, even when using fewer total elements. Moreover, P2 elements consistently outperform P1, particularly in configurations with short electrode separations, where field gradients are more intense. Tools such as *FEniCS* facilitate the selection of the polynomial interpolation order, enabling straightforward comparison between different finite element spaces.

Visualizations of modulation amplitude and absolute error across different configurations confirmed that the largest errors occur near singularities induced by point current sources and across tissue interfaces. Future work will extend this analysis to anatomically realistic head geometries and explore further comparisons between complete electrode models and point-source approximations using higher-order elements.

1 Introduction

Electrical stimulation mapping (ESM) plays a key role in presurgical evaluation of patients with drug-resistant epilepsy. In the context of stereoelectroencephalography (SEEG), ESM—referred to as depth electrical stimulation mapping (DESM)—is performed by delivering current through intracranial electrodes implanted directly within the brain tissue. Traditionally, DESM applies stimulation between adjacent electrode contacts to localize eloquent cortical regions and delineate the epileptogenic zone (EZ) [1]. While clinically valuable, this approach is spatially constrained and typically limited to direct activation near the electrode contacts.

Recently, temporal interference (TI) stimulation has emerged as a promising strategy to overcome such limitations. Originally proposed in the context of transcranial electrical stimulation (TES), TI leverages the spatial superposition of two high-frequency currents with slightly different frequencies to produce a low-frequency envelope that can modulate neural activity in deep brain regions, far from the electrodes themselves [2]. The amplitude of the envelope, known as modulation depth, is considered the strength of the stimulation. The concept of using all SEEG contacts as a programmable stimulation array opens new possibilities for enhancing focality and steering current distribution towards pre-defined regions of interest (ROIs) beyond adjacent contacts [3]. It is relatively common that there is some disagreement between the implanted electrode locations and some brain regions to stimulate, typically due to some imprecision in the electrode placement or to the appearance of new hypotheses after implantation. Implanting new electrodes inside the brain to increase the DESM coverage is both invasive and costly for the patient. Therefore, using TI with SEEG electrodes is clinically promising because it unlocks the possibility of stimulating a much larger number of brain regions, including regions not necessarily adjacent to the electrode contacts, without requiring additional implants.

To accurately evaluate the feasibility and precision of TI in intracranial stimulation contexts, robust computational modeling of the electric fields is required. Finite element method (FEM) solvers, combined with subject-specific head models, are commonly employed to solve Maxwell's equations in heterogeneous and anisotropic media. However, the numerical accuracy of FEM solutions depends critically on two factors: the spatial discretization of the domain (mesh resolution) and the polynomial degree of the basis functions used. New open source tools simplify the generation of inhomogeneous meshes that are refined in the ROIs and make it possible to change polynomial order in a straightforward manner [4].

In this work, taking advantage of modern finite element solvers and meshing tools, we investigate the impact of tetrahedral mesh refinement and polynomial degree (first and second order elements) on FEM simulations of temporal interference DESM. To serve as ground truth to validate the different FEM solutions, we derive and provide the analytical solution of the TI modulation depth for a four-point current injection in a multilayer spherical head model with three concentric spheres representing brain tissue, cerebrospinal fluid (CSF), and skull. Recent studies have demonstrated that point current injection provides a good approximation to the complete electrode model, especially when the ROI lies beyond the electrode itself [3].

We quantify the relative error across different meshes (homogeneous and refined with approximately 2, 5 and 9 million element) and polynomial order for different distances between the two current injections, and analyze how these affect the modulation depth of temporal interference within an ROI between the two electrode pairs. Our results provide insight into the optimal balance between computational cost and accuracy in FEM-based DESM simulations.

2 Methods

Assuming the quasi-static approximation of Maxwell's equations due to the low frequencies used in TI stimulation (less than 20kHz in TI applications) and using conductor theory, the electric potential Φ of one current injection pair in the absence of sources satisfies the Laplace equation [5]:

$$\nabla \cdot \sigma(\mathbf{r}) \nabla \Phi(\mathbf{r}, t) = 0, \quad (1)$$

where $\sigma(\mathbf{r})$ is the conductivity of the medium and may depend on the position. We assumed an isotropic medium, so $\sigma(\mathbf{r})$ is a scalar. When current is injected through point electrodes, current injection is modeled with Dirac delta distributions and it is assumed that the electric field applied by the electrodes is typically much larger than the fields generated by neuronal activity. If a two-point current with amplitude I is injected at positions \mathbf{r}_s (source) and \mathbf{r}_d (sink), the electric potential can be found by solving the Poisson equation [5]:

$$\nabla \cdot \sigma(\mathbf{r}) \nabla \Phi(\mathbf{r}, t) = I[\delta(\mathbf{r} - \mathbf{r}_s) - \delta(\mathbf{r} - \mathbf{r}_d)] \quad (2)$$

2.1 Three-layer spherical head model

A spherical model with three concentric layers is proposed to model the head. Each layer represents brain tissue, cerebrospinal fluid (CSF) and skull. The scalp layer is not needed because of the high CSF and low skull conductivity values that act as an electrical shield, and in the case of DESM, both the current sources and the ROIs are inside the brain. The different layers are labeled by i , ranging from 1 to 3. The symmetry of the proposed geometry allows us to find an analytical solution for intracranial stimulation, which is not possible for arbitrary geometries. Within each layer, the medium is assumed to be homogeneous, i.e., the conductivity $\sigma_i(\mathbf{r})$ is constant. The radii (R_1 , R_2 and R_3 for each interface from inner to outer) and conductivities used are listed in Table 1 [6].

The solution to equation (2) is subject to the Neumann boundary condition in the external layer:

$$\frac{\partial \Phi^3}{\partial r}(R_3) = 0 \quad (3)$$

This boundary condition implies that no current escapes the outer layer. Furthermore, the continuity of both electric potential and current across the layer boundaries must hold:

$$\Phi^{(i+1)}(R_i) = \Phi^{(i)}(R_i) \quad (4)$$

$$\sigma_{i+1} \frac{\partial \Phi^{i+1}}{\partial r}(R_i) = \sigma_i \frac{\partial \Phi^i}{\partial r}(R_i) \quad (5)$$

Table 1: Radii and conductivities used for each layer of the spherical head model.

Layer	Radius	Conductivity
Brain	$R_1 = 7.8 \text{ cm}$	$\sigma_1 = 0.33 \text{ S/m}$
CSF	$R_2 = 8.0 \text{ cm}$	$\sigma_2 = 6 \times \sigma_1 \text{ S/m}$
Skull	$R_3 = 8.5 \text{ cm}$	$\sigma_3 = \sigma_1 / 80 \text{ S/m}$

2.2 Analytical solution

The analytical solution can serve as a ground truth when it is compared to numerical methods like FEM. The solution to equation (2) subject to the boundary conditions (3, 4, 5) can be found in terms of spherical harmonics [5]. It is well known that the solution for the potential in free space for two-point current sources is [7]:

$$\Phi_{\infty}(\mathbf{r}) = \frac{I}{4\pi\sigma_i} \left(\frac{1}{|\mathbf{r} - \mathbf{r}_s|} - \frac{1}{|\mathbf{r} - \mathbf{r}_d|} \right) \quad (6)$$

We can use the superposition theorem to find the expansion of the solution. If we place the source over the z-axis, the system has azimuthal symmetry, i.e., the solution does not depend on the azimuthal angle. Without loss of generality, the same applies to the sink, as it is possible to rotate the system to align the z-axis with the sink, restoring azimuthal symmetry. Then, the electric potential only depends on the angles between a given point in space and the locations of the point source and sink (see Figure 1). The solution can be split into a homogeneous and a free-space (or unbounded) term:

$$\Phi^{(i)}(\mathbf{r}, \theta, \beta) = \Phi_{\infty}^{(i)}(\mathbf{r}) + \Phi_h^{(i)}(\mathbf{r}, \theta, \beta), \quad (7)$$

where the homogeneous part is :

$$\Phi_h^{(i)}(\mathbf{r}, \theta, \beta) = \sum_{l=1}^N \left(A_l^{(i)} \mathbf{r}^l + B_l^{(i)} \mathbf{r}^{-(l+1)} \right) P_l(\cos(\theta)) - \left(C_l^{(i)} \mathbf{r}^l + D_l^{(i)} \mathbf{r}^{-(l+1)} \right) P_l(\cos(\beta)) \quad (8)$$

The determination of the constants is determined by the boundary conditions (3, 4, and 5) and $P_n\{\cdot\}$ is the n th Legendre Polynomial. $\Phi^{(i)}$ indicates the electric potential in the i th layer.

The potential does not depend on the coordinate system, because $\cos(\theta)$ and $\cos(\beta)$ can be written in terms of the scalar product $\cos(\theta) = \hat{\mathbf{r}} \cdot \hat{\mathbf{r}}_b$ and $\cos(\beta) = \hat{\mathbf{r}} \cdot \hat{\mathbf{r}}_a$. Then, scalar products are invariant under rotations, and positions of the injection points are arbitrary inside the brain. The electric potentials can be computed for each of the two TI current injection pairs, the electric field can be obtained as the gradient of these potentials, and the modulation depths can be obtained using Grossman et al.'s [2] formula from the two interfering electric field spatial distributions.

The constants of the analytical solution are provided in Appendix A due to the length of their derivation.

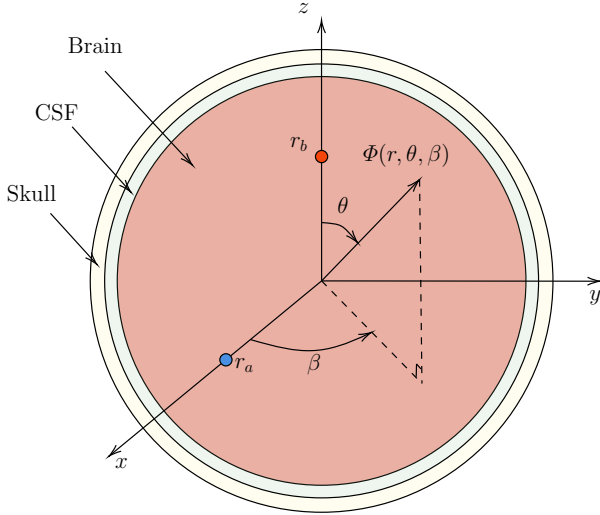


Fig. 1: Three-layer spherical head model. r_b and r_a are the locations of the source and sink respectively. The potential Φ only depends on \mathbf{r} and the angles between field and sources.

2.3 Finite Element Method

The finite element method (FEM) is a numerical technique for solving differential equations, especially useful in complex geometries and with arbitrary boundary conditions. To find the numerical solution for brain stimulation, we solved the Poisson equation (2). To compute the solution, we generated different 3D meshes to represent the three-layer spherical model. We used the open-source program *Gmsh* [8].

Multiplying by a test function v , integrating both sides of (2) in the domain Ω and considering that $\sigma(\mathbf{r})$ is constant we obtain the weak formulation of the problem:

$$\int_{\Omega} v (\sigma(\mathbf{r}) \nabla^2 \Phi(\mathbf{r}, t)) dx = I \int_{\Omega} v [\delta(\mathbf{r} - \mathbf{r}_s) - \delta(\mathbf{r} - \mathbf{r}_d)] dx \quad (9)$$

If we integrate the left side by parts and consider the homogeneous Neumann boundary condition on the surface $\partial\Omega$, we arrive at the weak formulation:

$$\int_{\Omega} \sigma(\mathbf{r}) (\nabla v \cdot \nabla \Phi) dx = I \int_{\Omega} v [\delta(\mathbf{r} - \mathbf{r}_s) - \delta(\mathbf{r} - \mathbf{r}_d)] dx \quad (10)$$

Mathematically, the left side of (10) is known as a bilinear form and the right as a linear form. The solution and the test functions v belong to the function space V , a Sobolev space $H^1(\Omega)$. We are interested in the finite-dimensional trial space $V_h \subset V$ and look for an approximation $\Phi_h \in V_h \subset V$. The weak

formulation allows the use of functions with discontinuous derivatives and piecewise polynomial function spaces; i.e., function spaces constructed by stitching together polynomial functions on simple domains such as tetrahedra [4]. We implemented the FEM in *FEniCS* [4]. *FEniCS* is an open-source computing platform for solving partial differential equations (PDEs) using the finite element method. It is written in C++ with a Python interface, combining high performance with a user-friendly syntax that allows researchers and engineers to implement complex models with minimal effort. Meshes and Lagrange finite elements of different orders were used to compute the potentials and the electric fields.

All simulations were performed on a personal workstation running Ubuntu 20.04.5 LTS, equipped with an Intel® Core™ i7-10700F CPU @ 2.90GHz (8 cores / 16 threads) and 128GB of RAM. The linear systems were solved using the PETSc Krylov solver, configured with the Conjugate Gradient method and an Incomplete LU (ILU) preconditioner. The residual norm was set to 10^{-8} .

2.4 Temporal interference electrical brain stimulation

The Temporal Interference (TI) method leverages the nonlinear response of neurons to amplitude-modulated electric fields generated by the superposition of two or more high-frequency sinusoidal currents. TI stimulation exploits interference patterns created by applying two slightly different high-frequency currents. While the individual carrier frequencies are too high to affect neuronal firing directly, the low-frequency envelope can modulate neural activity at depth. In patients with refractory epilepsy, one therapeutic option involves performing intracranial procedures with the implantation of depth electrodes (SEEG). These electrodes allow both the recording of brain activity and direct electrical stimulation between adjacent contacts located in specific brain regions, with the goal of modulating pathological neuronal activity and precisely locating epileptogenic zones. However, the stimulated area is restricted to the position of the electrodes. With TI, it is possible to stimulate other zones between different electrodes, thus enabling the identification of epileptogenic zones within a broader area (see Figure 2).

Grossman et al. (2017) provide a modulation depth formula at each location:

$$|\mathbf{E}_{AM}^{max}| = \begin{cases} 2|\mathbf{E}_2(\mathbf{r})| & \text{if } |\mathbf{E}_2(\mathbf{r})| \leq |\mathbf{E}_1(\mathbf{r})|\cos(\alpha) \\ 2\frac{|\mathbf{E}_2(\mathbf{r}) \times (\mathbf{E}_1(\mathbf{r}) - \mathbf{E}_2(\mathbf{r}))|}{|\mathbf{E}_1(\mathbf{r}) - \mathbf{E}_2(\mathbf{r})|} & \text{if } \text{otherwise} \end{cases} \quad (11)$$

where $\mathbf{E}_1(\mathbf{r})$ and $\mathbf{E}_2(\mathbf{r})$ are the electric fields produced by the first and second electrode pairs, respectively, and α is the angle between the electric fields, assumed to be in $[0, \pi/2]$ without loss of generality.

We simulated various stimulation scenarios for different electrode pair spacings $d = 1, 2, 3, 4, 5$ cm. For each configuration, we computed the electric field and extracted the maximal modulation amplitude using both the FEM and analytical models. The relative error was then evaluated within a predefined region of interest (ROI). The ROI was chosen to be close to the injection sites, assuming

a source separation of $s = 1$ cm. It was defined as an ellipsoid centered between the four current injection points at $(0, 0, 6.5)$ cm, and its formula is given by:

$$x^2 + y^2 + \frac{(z - 6.5)^2}{\sqrt{3}} = 1 \quad (12)$$

All calculations of relative error were performed only within this ellipsoidal ROI.

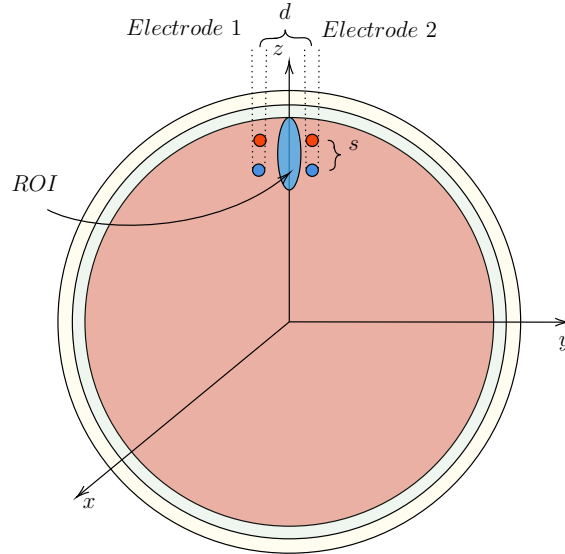


Fig. 2: Two electrodes (four contacts) are used to stimulate, generating each one electric field (corresponding to one frequency). The region of interest (ROI) is an ellipsoid between the electrodes, where the best alignment between the two fields and thus the largest modulation depth occur. The distance between electrodes is d and the distance between contacts is s .

2.5 Uniform and Refined Meshes

The quality, resolution, and refinement strategy of the mesh directly influence the accuracy and convergence of the numerical solution. In this work, we employed both uniform meshes, with evenly distributed elements throughout the brain domain, and locally refined meshes, which have denser elements in regions where higher spatial resolution is required (e.g., near the current injection sites and the ROI). Tetrahedral elements were chosen for meshing the multi-layer spherical model due to their flexibility in accurately representing curved tissue interfaces and allowing local mesh refinement, which also makes tetrahedral elements one of the most popular element shapes for electromagnetic brain

simulations. Moreover, Gmsh offers robust and optimized algorithms for generating unstructured tetrahedral meshes, such as Delaunay and Frontal-Delaunay methods, which integrate seamlessly with the FEniCS framework used in this study.

By maintaining a similar total number of elements across both mesh types, we aimed to isolate the effect of mesh refinement strategy from that of polynomial interpolation order on the simulation accuracy. We computed the modulation depth for six different meshes, keeping the total number of elements within the same order of magnitude to ensure a fair comparison. The meshes were generated by varying the characteristic element length. To improve the accuracy of the solution, local mesh refinement was applied in spherical regions surrounding the point current injection sites and the ROI (see Figure 3). Table 2 in Appendix B summarizes the coordinates of all points where local refinement was applied to increase spatial resolution near the sources.

Refined meshes contained approximately 1.64 million (2M), 4.59 million (5M), and 8.28 million (9M) elements, while uniform meshes contained around 1.5 million (2M), 4.31 million (5M), and 8.93 million (9M) elements. For simplicity, we refer to each mesh by the nearest upper bound in millions of elements (e.g., 2M for a mesh with approximately two million elements). We compared all FEM results against the analytical solutions evaluated at the same nodes.

All generated meshes were subject to the built-in quality optimization procedures in Gmsh, which discard poorly shaped tetrahedra based on internal heuristics. To further ensure the reliability of our discretizations, we computed the worst element quality in each mesh using standard shape metrics available in mesh processing tools (e.g., `meshquality` from `iso2mesh` [9]). Across all configurations, the worst quality values remained above 0.10, indicating the absence of highly distorted elements that could compromise numerical stability.

3 Results

We computed the relative error in the ellipsoidal ROI (12) with the following metric:

$$\text{Error}[\%] = \frac{\text{mean}(|\mathbf{E}_{AM}^{\max}|_{FEM} - |\mathbf{E}_{AM}^{\max}|_{Analytic})}{\text{mean}(|\mathbf{E}_{AM}^{\max}|_{Analytic})} \quad (13)$$

Figure 4 summarizes the relative error in the modulation depth across all tested configurations, using a consistent logarithmic color scale to allow direct comparison. The plot includes both uniform and locally refined meshes with approximately 2M, 5M, and 9M elements, combined with linear (P1) and quadratic (P2) Lagrange basis functions. As expected, increasing the total number of elements in a uniform or refined mesh leads to improved accuracy. Interestingly, P2 elements outperform P1 elements, even with coarser meshes, and this is one of the most important findings of this work. Locally refined meshes consistently achieve lower relative errors, even with similar element counts, due to their ability to better resolve the steep electric field gradients near the current injection

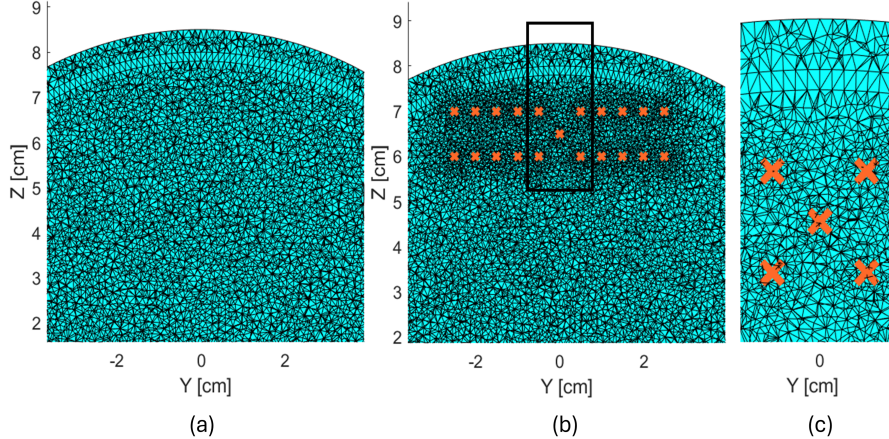


Fig. 3: Comparison between the uniform and locally refined mesh configurations. For clarity, only the 5M meshes are shown. (a) Uniform mesh. (b) Locally refined mesh. Orange crosses indicate the refinement points (see Table 2 in Appendix B). (c) Zoomed view of the black box in panel (b), illustrating the increased resolution around the refinement region.

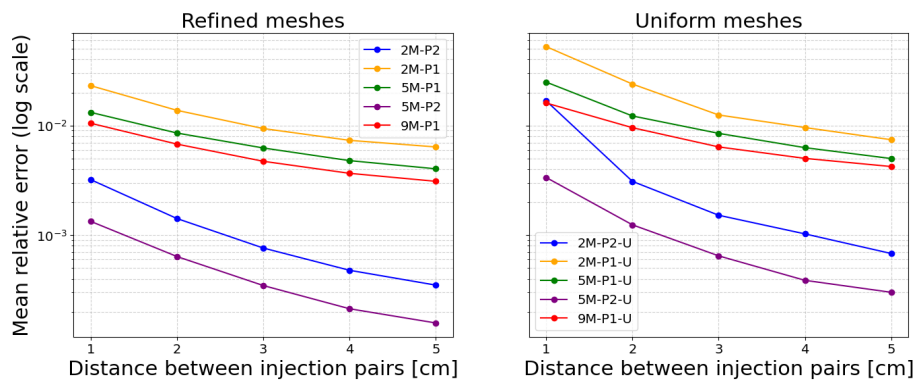


Fig. 4: Relative error of the modulation depth in the ellipsoidal ROI as a function of the electrode pair separation, comparing different finite element discretizations. Results are shown for three mesh sizes (2M, 5M, 9M elements), each implemented in two variants: uniform mesh and locally refined mesh near the stimulation region. For each mesh, both linear (P1) and quadratic (P2) Lagrange elements were evaluated. These results demonstrate convergence behavior both with increasing mesh resolution and with higher-order polynomial interpolation.

sites. This highlights the importance of co-optimizing mesh refinement and interpolation order to improve simulation accuracy in temporal interference electrical brain stimulation.

When using quadratic (P2) elements, significantly higher accuracy was achieved—particularly for the 1 cm separation case—where the largest errors occur near the singularities introduced by point current injection. This improvement is attributed to the higher-order approximation of P2 elements, which allows them to better capture curvature and steep gradients, especially near the sources where the electric potential changes rapidly. Modulation depth was plotted for the

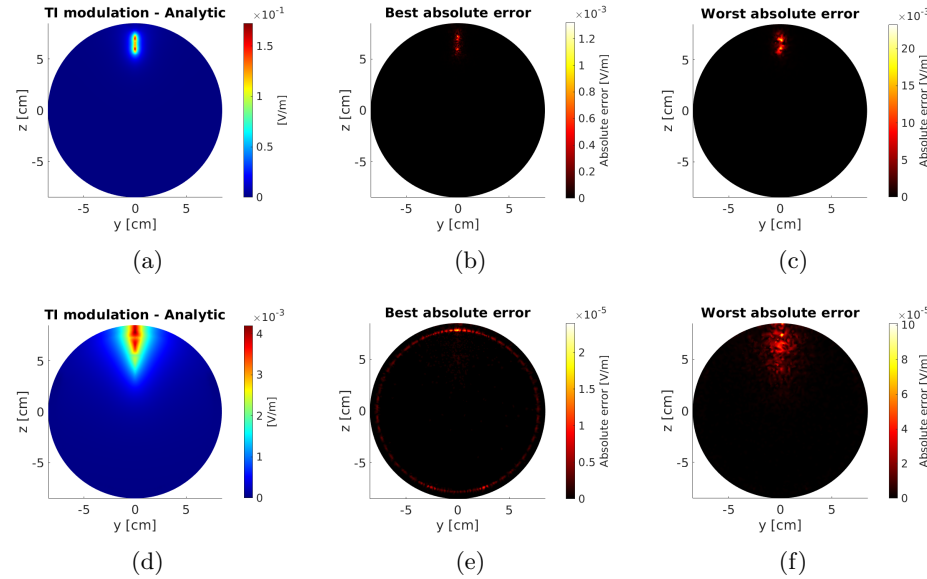


Fig. 5: (a) Analytical solution for the configuration with 5 million elements and electrode separation $d = 1\text{ cm}$. (b) Absolute error using FEM with P2 elements on the 5M refined mesh (best case). (c) Absolute error using FEM with P1 elements on a uniform 2M mesh (worst case). (d) Analytical solution for the configuration with 5 million elements and electrode separation $d = 5\text{ cm}$. (e) Best FEM result using P2 elements on the 5M refined mesh. (f) Worst FEM error using a uniform 2M mesh and P1 elements. Note that the colorbar scales differ between (b), (c), (e), and (f), each adapted to the corresponding maximum error.

smallest and largest electrode separations. For comparison, the absolute errors of the best and worst FEM configurations were also included. These two cases are illustrated in Figure 4: the best case corresponds to a 5M refined mesh with P2 elements, while the worst case corresponds to a 2M uniform mesh with P1 elements.

In Figure 5, the region of interest (ROI) was defined by considering the location of maximum modulation depth produced with the minimum electrode separation. As the injection pairs are moved farther apart, the location of the maximum modulation amplitude shifts toward the cerebrospinal fluid (CSF) region. For the largest separation distance, the highest modulation amplitude is located in the CSF and no longer within the defined ROI. This shift is due to the fact that, at larger separations, the point current injections are located closer to the CSF boundary.

Regarding the error in the best FEM case, it is clear that the discrepancy is not limited to the region of maximum modulation. This behavior is attributed to limitations in the analytical solution itself. The truncation of the series in Equation 8 introduces mismatches in the potential continuity across tissue interfaces. In this case, we used $N = 150$ terms of the summation, and the error remained below 3×10^{-5} (see subfigure (e) in Figure 5). Additional terms can be included in the summation if higher accuracy is required for the application of interest.

These cases further support the observations in Figure 4, demonstrating that high-order elements combined with local mesh refinement significantly reduce the error across the entire domain—not just near the electrodes—while uniform meshes with low-order elements produce larger and more spatially diffuse errors.

4 Discussion

This study investigated the trade-off between mesh refinement and interpolation order in FEM simulations of temporal interference (TI) brain stimulation. We compared six mesh configurations—three uniform and three locally refined—while maintaining a comparable total number of elements to ensure a fair comparison.

The results demonstrated that simply increasing the total number of elements in a uniform fashion does not guarantee improved accuracy. In contrast, locally refined meshes produced significantly lower relative errors in the region of interest (ROI), particularly when the electric field exhibited steep spatial gradients near current injection sites. This highlights the importance of allocating mesh resolution strategically, rather than uniformly, to capture the physical behavior of the system more effectively.

Moreover, higher-order polynomial elements (P2) consistently outperformed linear elements (P1) across all mesh configurations—one of the key findings of this study. This was especially evident in the case of short electrode separations (e.g., $d = 1$ cm), where singularities in the point current model lead to sharp field variations. P2 elements, with their ability to represent curvature and more complex field variations, were able to capture these effects with greater fidelity.

The combination of moderate mesh refinement and P2 elements achieved comparable—or even superior—accuracy compared to extremely dense uniform meshes using P1 elements, while requiring similar computational resources. For instance, computing the solution with P2 elements on the 2M refined mesh took approximately 29 minutes, compared to 23 minutes for the 9M uniform mesh

with P1 elements, both run on the same machine. This additional time is explained by the increased number of degrees of freedom associated with higher-order elements. These findings support the notion that mesh design and polynomial interpolation order should be co-optimized for performance and computational costs rather than considered independently.

In practice, this has important implications for FEM-based patient-specific modeling of DESM with TI. Clinical applications require a balance between model accuracy and simulation time. Our results suggest that combining adaptive mesh refinement near the stimulation region with higher-order basis functions can yield more accurate electric field estimates without incurring excessive computational cost. Importantly, this study introduces a novel analysis focused on the error in the modulation depth formula of Equation 11, which incorporates both the gradient-based computation of the electric field and the combination of the two interfering fields. This goes beyond prior studies that primarily assessed the accuracy of the electric potential alone [10], offering more clinically relevant insights.

Finally, by validating our FEM results against an analytical solution derived from a multilayer spherical head model, we assessed the reliability of the numerical implementation to be used in realistic, patient-specific head models which is our next step. Although this study is based on a simplified geometry with known ground truth, the main findings—such as the benefits of local mesh refinement and higher-order interpolation near regions of high field gradients—are expected to be generalizable to anatomically realistic head models. In such complex domains, high electric field variations often arise near tissue interfaces or electrode contacts.

5 Conclusions

In this work, we evaluated the influence of mesh refinement and polynomial interpolation order on the accuracy of FEM simulations for temporal interference (TI) electrical brain stimulation. Using a multilayer spherical head model with an analytical solution as ground truth, we assessed the relative error in the FEM-based estimation of maximum modulation depth within a predefined region of interest (ROI).

Our results indicate that local mesh refinement near the current injection sites significantly improves accuracy while avoiding excessive mesh density throughout the domain. Furthermore, higher-order elements consistently outperform linear elements (P1), particularly in regions with steep potential gradients induced by point sources.

Future work will extend this analysis to anatomically realistic head models. Additionally, we will explore further comparisons between the complete electrode model and the point-source approximation, focusing on simulations with P2 elements. The findings presented here suggest that improved precision near the electrodes may be achievable, potentially providing more accurate estimations than those reported in [3].

References

1. Trébuchon, A., Chauvel, P.: Electrical stimulation for seizure induction and functional mapping in stereoelectroencephalography. *Journal of Clinical Neurophysiology* 33(6), 511–521 (December 2016), <https://doi.org/10.1097/WNP.0000000000000313>, review article
2. Grossman, N., Bono, D., Dedic, N., Kodandaramaiah, S.B., Rudenko, A., Suk, H.J., Cassara, A.M., Neufeld, E., Kuster, N., Tsai, L.H., Pascual-Leone, A., Boyden, E.S.: Noninvasive deep brain stimulation via temporally interfering electric fields. *Cell* 169(6), 1029–1041.e16 (06 2017), <https://doi.org/10.1016/j.cell.2017.05.024>
3. Collavini, S., Fernández-Corazza, M., Oddo, S., Princich, J.P., Kochen, S., Muravchik, C.H.: Improvements on spatial coverage and focality of deep brain stimulation in pre-surgical epilepsy mapping. *Journal of Neural Engineering* 18(4), 046004 (mar 2021), <https://dx.doi.org/10.1088/1741-2552/abe5b9>
4. Logg, A., Mardal, K.A., (Eds.), G.N.W.: Automated Solution of Differential Equations by the Finite Element Method: The FEniCS Book, Lecture Notes in Computational Science and Engineering, vol. 84. Springer (2012)
5. Jackson, J.D.: Classical electrodynamics. Wiley, New York, NY, 3rd ed. edn. (1999), <http://cdsweb.cern.ch/record/490457>
6. Næss, S., Chintaluri, C., Ness, T.V., Dale, A.M., Einevoll, G.T., Wójcik, D.K.: Four-sphere head model for eeg signals revisited. *bioRxiv* (2017), <https://www.biorxiv.org/content/early/2017/04/06/124875>, preprint
7. Frank, E.: Electric potential produced by two point current sources in a homogeneous conducting sphere. *Journal of Applied Physics* 23(11), 1225–1228 (11 1952), <https://doi.org/10.1063/1.1702037>
8. Geuzaine, C., Remacle, J.F.: Gmsh: A 3-d finite element mesh generator with built-in pre- and post-processing facilities. *International Journal for Numerical Methods in Engineering* 79(11), 1309–1331 (2009)
9. Fang, Q., Boas, D.A.: Tetrahedral mesh generation from volumetric binary and gray-scale images. In: IEEE International Symposium on Biomedical Imaging (ISBI). pp. 1142–1145 (2009)
10. Fernández-Corazza, M., Turovets, S., Price, N., Lu, P., Tucker, D., Muravchik, C., Malony, A.: Validation of forward solvers accuracy in EEG, EIT and TES. (2017)

A Constants in the analytical solution

The expressions for the constants found for the analytical expansion of the homogeneous potential Φ_h are:

$$s_{21} = \frac{\sigma_2}{\sigma_1}$$

$$s_{32} = \frac{\sigma_3}{\sigma_2}$$

$$R_{32} = \frac{R_3}{R_2}$$

$$K_1 = \frac{I}{4\pi\sigma_1}$$

$$L_1 = \frac{l+1}{l}$$

$$L_2 = 2l + 1$$

$$B = \frac{l}{L_2} \left(\frac{L_2}{l} - (1 - s_{32}) \right) + \frac{l}{L_2 L_1} R_{32}^{L_2} \left(\frac{L_2}{l} - (1 + s_{32} L_1) \right)$$

$$C = l \left(\frac{R_2^{L_2}}{L_2} (1 - s_{32}) + \frac{R_3^{L_2}}{L_2} \left(\frac{1}{L_1} + s_{32} \right) \right)$$

where R_i are the radii of the spherical layers, σ_i their corresponding conductivities, r_a and r_b the distances from the origin to the source and sink stimulation points, respectively, I the amplitude of the injected current, and l the index in the spherical harmonics summation. With the constants defined above, we obtain the expressions for the terms involved in the analytical potential solution:

$$\begin{aligned}
A_l^{(3)} &= K_1 \cdot \frac{L_2}{l} \cdot \frac{r_b^l}{B(1 - s_{21})R_1^{L_2} + C(1 + s_{21}L_1)} \\
A_l^{(2)} &= A_l^{(3)} \cdot B \\
B_l^{(2)} &= A_l^{(3)} \cdot C \\
A_l^{(1)} &= A_l^{(2)} + B_l^{(2)} \cdot R_1^{-L_2} - K_1 \cdot \frac{r_b^l}{R_1^{L_2}} \\
B_l^{(3)} &= \frac{1}{L_1} \cdot A_l^{(3)} \cdot R_3^{L_2} \\
C_l^{(3)} &= K_1 \cdot \frac{L_2}{l} \cdot \frac{r_a^l}{B(1 - s_{21})R_1^{L_2} + C(1 + s_{21}L_1)} \\
C_l^{(2)} &= C_l^{(3)} \cdot B \\
D_l^{(2)} &= C_l^{(3)} \cdot C \\
C_l^{(1)} &= C_l^{(2)} + D_l^{(2)} \cdot R_1^{-L_2} - K_1 \cdot \frac{r_a^l}{R_1^{L_2}} \\
D_l^{(3)} &= \frac{1}{L_1} \cdot C_l^{(3)} \cdot R_3^{L_2}
\end{aligned}$$

B Refinement points table

Table 2: Refinement points added near the stimulation region to increase mesh resolution.

Point ID	x [cm]	y [cm]	z [cm]
refine_p0	0	0	6.5
refine_p1	0	0.5	7.0
refine_p2	0	0.5	6.0
refine_p3	0	1.0	7.0
refine_p4	0	1.0	6.0
refine_p5	0	1.5	7.0
refine_p6	0	1.5	6.0
refine_p7	0	2.0	7.0
refine_p8	0	2.0	6.0
refine_p9	0	2.5	7.0
refine_p10	0	2.5	6.0
refine_p11	0	-0.5	7.0
refine_p12	0	-0.5	6.0
refine_p13	0	-1.0	7.0
refine_p14	0	-1.0	6.0
refine_p15	0	-1.5	7.0
refine_p16	0	-1.5	6.0
refine_p17	0	-2.0	7.0
refine_p18	0	-2.0	6.0
refine_p19	0	-2.5	7.0
refine_p20	0	-2.5	6.0